

Key Points:

- Global variabilities of the mean I-T due to tidal and solar-magnetospheric (SM) forcing are described, analyzed and quantified
- Both circulation systems occupy the full latitude-height domain, and consist of local, regional and global cellular-like structures
- Ne variability occurs through O/N₂ via tidal-forced temperatures, and mainly by solar flux changes for the SM-forced I-T

Supporting Information:

Supporting Information may be found in the online version of this article.

Correspondence to:

J. M. Forbes,
forbes@colorado.edu





Citation:

Forbes, J. M., Zhang, X., Maute, A., & Cullens, C. (2024). Responses of the mean thermosphere circulation, O/N₂ ratio and Ne to solar and magnetospheric forcing from above and tidal forcing from below. *Journal of Geophysical Research: Space Physics*, 129, e2024JA032449. <https://doi.org/10.1029/2024JA032449>

Received 12 JAN 2024

Accepted 6 MAR 2024

Responses of the Mean Thermosphere Circulation, O/N₂ Ratio and Ne to Solar and Magnetospheric Forcing From Above and Tidal Forcing From Below

Jeffrey M. Forbes¹ , Xiaoli Zhang¹ , Astrid Maute² , and Chihoko Cullens³ 

¹Ann and H.J. Smead Department of Aerospace Engineering Sciences, University of Colorado, Boulder, CO, USA,

²Cooperative Institute for Research in the Environmental Sciences (CIRES), University of Colorado, Boulder, CO, USA,

³Laboratory for Atmospheric and Space Physics (LASP), University of Colorado, Boulder, CO, USA

Abstract The day-to-day variability (“weather”) associated with the diurnal- and zonal-mean (DZM) circulation, O/N₂ ratio and electron density (Ne) of the I-T system due to tidal “forcing from below” and solar flux and magnetosphere (SM) “forcing from above” during 2021 are delineated, diagnosed and quantitatively compared using a series of model simulations designed to separate these responses with respect to their origins. The external forcings are driven by actual tidal, solar wind, and solar flux observations. Both circulation systems occupy the full extent of the I-T, and the SM-forced DZM circulation is 2–3 times more vigorous in terms of vertical and meridional wind magnitudes. Tidal-driven DZM Ne reductions of up to 30%–40% with respect to those of the fully forced I-T system occur, mainly between ±30° latitude, compared to SM-driven increases of up to 15%–20%. In terms of annual variances over this latitude range, tidal-driven DZM Ne variances exceed or equal those of the SM-driven variances. The former is mainly controlled by O/N₂ ratio vis-a-vis tidal-forced temperature variations above 150 km. While a similar cause-effect relation exists for the latter, this is superseded by Ne variability associated with solar production. However, DZM I-T system variability forced from below is underestimated in the simulations in two respects: the effects of gravity waves are omitted, and tidal forcing is represented by 45-day running means, as compared with the more realistic actual daily variability of SM forcing. These shortcomings should be ameliorated once multi-satellite missions planned for the future come to fruition.

1. Introduction

Forcing “from above” on ionosphere-thermosphere (I-T) space weather refers to variable solar EUV flux, and solar wind variability channeled through coupling of the I-T system with the magnetosphere. Forcing “from below” refers to the spectrum of gravity waves (GWs), tides and planetary waves (PWs) propagating up from atmospheric regions below ~100 km altitude, and that exert their influence on the I-T system through a variety of processes. However, it is challenging to compare and quantify the relative consequences of forcing from above and below. In this paper we address this topic with focus on the special case of the mean I-T circulation and electron density (Ne) responses to solar flux and magnetospheric forcing from above, and tidal forcing from below, at low to moderate levels of solar activity. In the following paragraphs, additional context and motivation for this study are provided.

The diurnal- and zonal-mean circulation (hereafter “DZM circulation”) is a fundamental dynamical component of planetary atmospheres. It manifests in the meridional plane in the form of cellular-like circulations driven by differential solar heating and/or momentum sources associated with dissipating waves. In Earth’s lower atmosphere, the Hadley cell is an example of a heat-driven “thermally direct” circulation (James, 2002). Warm air rises at the equator, flows poleward at about 10–15 km in both hemispheres, descends near ~±30° latitude where it has cooled sufficiently to sink, and flows equatorward near the surface to close the cell. The Coriolis force acting on the near-surface winds gives rise to the familiar trade winds.

An example of a wave-driven circulation exists in Earth’s mesosphere, between about 50 and 95 km altitude (see, e.g., Andrews et al., 1987, and the seminal works of Lindzen (1981) and Holton (1983)). Eastward (westward) jets in the winter (summer) hemisphere between 20 and 80 km filter out much of the eastward-(westward-) part of the vertically propagating gravity wave (GW) spectrum, leaving the remaining westward (eastward) GWs to dissipate between 80 and 95 km and deposit mean momentum, which has several consequences. First, since the deposited

momentum is opposite in direction to that of the underlying jets, the jets are decelerated in this region, and moreover secondary jets of opposite direction occur. The divergence of momentum flux furthermore represents a force on the atmosphere that is balanced in the steady-state zonal momentum equation by a summer-to-winter flow vis-a-vis the Coriolis effect. In the meridional plane, continuity requires upward(downward) motions at middle to high latitudes in the summer(winter) hemisphere. The accompanying adiabatic cooling(heating) produces colder(warmer) temperatures in summer(winter) and a meridional temperature gradient opposite to that expected on the basis of radiative equilibrium.

Recent modeling and observational evidence, with origins in the seminal numerical modeling of Miyahara (1978), points to additional “lower-thermosphere (LT) circulation” cells between about 105 and 130 km altitude that are mainly driven by tides and inertia gravity waves, with GWs playing a secondary role (J. C. Wang et al., 2002, and references therein). During solstice the LT circulation simulated in Wang et al. (2022) consists mainly of a single reversed cell with respect to the mesospheric circulation just described. Qian and Yue (2017) demonstrate the importance of the LT circulation to the seasonal-latitudinal distribution of the O/N_2 ratio in the thermosphere, and consequently on the ionosphere. Qian et al. (2017) furthermore demonstrate the importance of the LT circulation on the DZM distribution of CO_2 , and in fact N. Wang et al. (2022) use the CO_2 distribution to infer the DZM LT circulation.

From a historical perspective, the first simulations of the DZM circulation in the full thermosphere domain (Dickinson et al., 1975, 1977) focused on altitudes of order 150–600 km, and included solar heating, high-latitude Joule heating, and a parameterized momentum source due to the interaction of the diurnal tidal winds and diurnal ion drag. The primary solstitial circulation in their work is thermally direct, that is summer to winter in line with the latitudinal distribution of heating. The corresponding equinoctial circulation is similar to the Hadley cell described earlier, except more global in extent. In that work the high-latitude heating created a circulation cell opposing that of the equinoctial cell, with transition between the two occurring over a broad range of latitudes depending on the strength of the high-latitude heating. The high-latitude-driven circulation cell similarly opposes that of the solar-driven solstitial cell in the winter hemisphere, but reinforces the solar-driven cell in the summer hemisphere.

Following the work of Dickinson et al. (1975, 1977), various studies demonstrated that dissipation of diurnal and semidiurnal solar tides created a DZM LT circulation with cellular-like features (e.g., Angelats i Coll & Forbes, 2002; Miyahara, 1978; Miyahara & Wu, 1989; Yoshikawa & Miyahara, 2003). Subsequent studies (e.g., Forbes et al., 1993; Jones, Jr. et al., 2014; Yamazaki & Richmond, 2013) elucidated the compositional effects that accompany tidal dissipation. Recent modeling (e.g., Miyoshi & Yiğit, 2019) also suggests that GW dissipation makes non-negligible contributions to the thermosphere circulation. However, while the climatological spectrum of tides entering the thermosphere is now reasonably well known observationally (e.g., Forbes et al., 2003, 2008; Truskowski et al., 2014; Yamazaki et al., 2023), the spectrum of GWs entering the thermosphere from below remains to be adequately defined.

In this paper the term “cellular-like” loosely refers to clockwise and counter-clockwise motions in the meridional plane (pole-to-pole, 100–400 km altitude) that range in horizontal scale from regional (~500–5,000 km) to global, and vertical extents ranging from 10 to 400 km. And, contrary to the Hadley circulation which is for the most part a *closed cell* as defined above, many of the thermosphere flows that we will refer to as cellular-like are not closed. This is because smaller cellular-like features are embedded within larger ones, and their flows are linked. Smaller neighboring cellular-like features can similarly share common flows and thus might be termed *open*.

The remainder of this paper is focused on characterizing, diagnosing and comparing the DZM thermosphere circulations, O/N_2 ratios, and electron densities (Ne) as a function of height (100–400 km), latitude (90°S–90°N) and day of year (DOY, 1–365) due (a) solely to observation-based tides propagating up from below 100 km altitude, and (b) solely due to solar flux and magnetospheric (hereafter “SM”) forcing. This is accomplished using the version of the Thermosphere Ionosphere Electrodynamics General Circulation Model (TIEGCM) developed for the Ionospheric CONnections (ICON) mission, TIEGCM-ICON (Maute, 2017; see also Maute et al., 2023), which is forced at its lower boundary by the observed tidal spectrum; and an additional simulation with this tidal forcing omitted, supplemented by a third simulation with variable SM forcing replaced by constant SM forcing. The details of how these model results are manipulated to achieve our end goals is described in the next Section. Results are presented in Section 3, and conclusions are enumerated in Section 4.

2. Methodology

TIEGCM-ICON is described in detail in Maute (2017) and a useful summary is provided in Maute et al. (2023); therefore only a brief description is provided here. The TIEGCM self-consistently solves the momentum, energy, continuity and state equations of the thermosphere and ionosphere with coupled chemistry and electrodynamics (e.g., Qian et al., 2014; Richmond, 1995). In the TIEGCM-ICON implementation (Maute, 2017; Maute et al., 2023; see also Cullens et al., 2020; Forbes et al., 2017), the model is driven at its 97 km lower boundary by the spectrum of diurnal and semidiurnal tides derived from winds and temperatures measured by the Michelson Interferometer for Global High-Resolution Thermospheric Imaging (MIGHTI) instrument on ICON. Similar to the methodology underlying the Climatological Tidal Model of the Thermosphere (CTMT, Oberheide et al., 2011), this is accomplished by fitting Hough Mode Extensions (HMEs, Forbes & Zhang, 2022, and references therein) to the MIGHTI tidal fields between 10°S and 40°N latitude and 94–102 km altitude within 45-day windows slipped forward 1 day at a time. The 45-day windows are necessitated by the fact that complete longitudinal *and* local time coverage are required to extract the tidal spectrum, and given the orbital sampling of ICON/MIGHTI, this is only achieved for the above latitude range within ≈ 45 -day windows. The HME fits are used to generate hourly perturbation winds, temperatures and geopotential heights as a function of longitude and latitude (pole-to-pole) for input into the TIEGCM.

The tidal spectrum imposed at the lower boundary of TIEGCM-ICON includes diurnal tides from DE3 to DW2 and semidiurnal tides from SE3 to SW4. Here DE3 refers to “Diurnal Eastward-propagating tide with zonal wavenumber $s = -3$,” SW4 refers to “Semidiurnal Westward-propagating tide with zonal wavenumber $s = +4$,” and so on, where $s < 0$ ($s > 0$) refers to eastward (westward) propagation. The largest tides specified at the model boundary are the Sun-synchronous tides DW1 and SW2, and the solar-asynchronous DE3. For reference, they are illustrated in Figure S1 in Supporting Information S1 to this manuscript for the last full calendar year (2021) of data for the ICON mission, which is the focus of the present study. The salient features of the tidal lower boundary forcing lack significant inter-annual variability and are consistent with the CTMT.

To isolate the DZM circulation, O/N₂ and Ne only due to tidal forcing, two simulations are used, one with tidal/HME forcing at the lower boundary and one without tidal forcing, both including SM forcing. Taking grid point-by-grid point hourly “difference fields” between the two allows one to remove the effects of SM forcing, and to isolate the effects of tides on the overlying I-T system. The DZM components of various dependent variables are obtained by averaging them with respect to longitude and local time at each hourly latitude-height grid point. The notations used to identify each of the above-described DZM model outputs are “SM + tidal,” “SM” and “tidal” according to their forcing origins. The nature of this study is such that it is not possible to separate the relative influences of these and other tides forced at the TIEGCM lower boundary.

In the high-latitude region, magnetosphere-ionosphere coupling is simulated by specifying the ion convection pattern based on Weimer (2005) driven by solar wind data, that is, interplanetary magnetic field (IMF) B_y and B_z , solar wind velocity and pressure. The auroral precipitation is based on the analytical model by Roble and Ridley (1987) with parametrization by Emery et al. (2012). Solar EUV forcing is based on Richards et al. (1994).

In this paper we utilize a third TIEGCM-ICON product wherein the solar EUV flux and high-latitude forcing are set equal to constants throughout the year and HME tidal forcing is included. For this “conSM + tidal”-designated simulation, the solar EUV spectrum is fixed consistent with an 81-day mean value of 71 s.f.u. for the 10.7-cm radio flux (F10.7). The hemispheric power is fixed at 12 GW; solar wind velocity at 400 km/s; solar wind density at 4/cm³; IMF $B_y = B_x = 0$ and IMF $B_z = 1$ nT; cross-polar cap potential (CCP) at 33 kV. By taking difference fields between the HME-forced simulations with variable and fixed SM forcings (“SM + tidal” minus “conSM + tidal”) enables removal of the tidal-forced contribution, and isolation of the day-to-day variability of the mean circulation response to only SM forcing, relative to the seasonal-latitudinal climatology driven by constant SM forcing. This day-to-day variability (i.e., “weather”) associated with daily solar flux and magnetospheric variability is designated SM'. Again, diurnal and local-time averages are taken at each height-latitude grid point to obtain the DZM values of variables.

Figure 1 illustrates daily mean CCP and 10.7-cm solar flux values for 2021. After DOY 180 a quasi-27-day oscillation is evident in F10.7, indicating the presence of active regions on the Sun. After DOY 240 there is some degree of correlation between CCP and F10.7, but prior to DOY 180 geomagnetic activity remains rather elevated while solar fluxes on only a few days fall below the above reference value of 71 s.f.u.

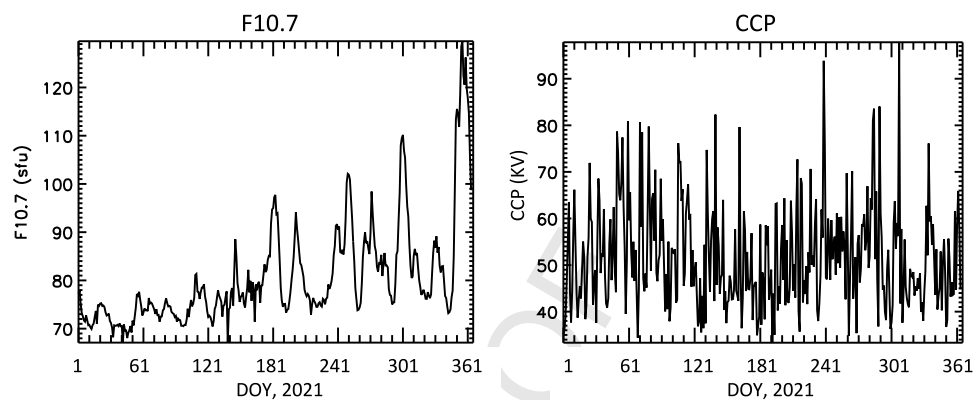


Figure 1. Daily F10.7 and cross-polar cap potential (CCP) used in the SM-forced calculations.

All hourly DZM fields to be presented in this paper are depicted in geographic and height coordinates, which is arguably the most intuitive and practical organization of data for the purposes of quantifying I-T “weather.” The tidal-driven results represent the responses to 45-day running-mean tidal forcing at 97 km for the reasons given previously, and the SM-forced results represent the daily mean responses to forcing at the 30-s temporal resolution of the TIE-GCM. The goal of the following two subsections is to provide descriptions of the main features of the DZM circulations driven from above and below, to provide some interpretations, and to provide context for Section 4, where quantitative comparisons between the variabilities of the I-T system driven from above and from below are provided.

3. Results

The variables of interest here are DZM eastward (U_n), northward (V_n), vertical (W_n) winds and temperatures (T_n), O/N_2 density ratio, and electron density (N_e). When referring to these variables, hereafter it is understood that these are DZMs.

3.1. DZM Circulation, O/N_2 and N_e Forced From Below

As will be noted below, there are several aspects of the results to be presented in this subsection that can be found in Jones et al. (2014, 2016, 2019). They performed similar studies wherein lower boundary forcing of the TIE-GCM was defined by HME tidal forcing based on winds and temperatures measured by the TIMED mission in the form of the Climatological Tidal Model of the Thermosphere (CTMT, Oberheide et al., 2011). These works are distinguished by their in-depth analyses of the source terms in the DZM momentum and thermal energy equations that define the DZM circulation due to dissipating tides, which provide a basis for interpreting and understanding the present results. Of particular note, the veracity of CTMT-based TIEGCM tidal solutions above 97 km were validated in Jones et al. (2014).

Figure 2 presents depictions of the tidal-driven U_n and V_n winds. The latitude versus day-of-year (latvsdo) structures and magnitudes of U_n do not vary appreciably between 150 km (Figure 2b) and 350 km (Figure 2a). Equatorward of $\pm 60^\circ$ latitude, these U_n responses likely mainly reflect the combined effects of DW1, SW2 and DE3 (Jones et al., 2014). Of particular note, the westward maxima in U_n of order -20 to -30 ms^{-1} near the equator correlate very well with the DW1 temperature maxima (Figure S1 in Supporting Information S1) that occur at the equator, consistent with the contention of Jones et al. (2019) that heat flux divergences are playing an important role. The westward forcing maximizes in the lower thermosphere where the tides dissipate, and the response is carried to the upper thermosphere through molecular diffusion. Following Jones et al. (2016) who focused on the September equinox period, Figure 2c provides a height-latitude slice of U_n magnitudes for DOY 271. Whereas the westward wind imprint near the equator decreases with height from a maximum value of 53 m/s, the flanking eastward wind regimes increase with height to ~ 6 –18 m/s, suggesting that these are either generated by dissipation of long-vertical wavelength tides that extend above 200 km, and/or that these tidal components interact with ion drag to generate a net eastward momentum source (Dickinson et al., 1975, 1977). Referring back to Figure 2a, these 3-peaked latitude structures appear mainly during

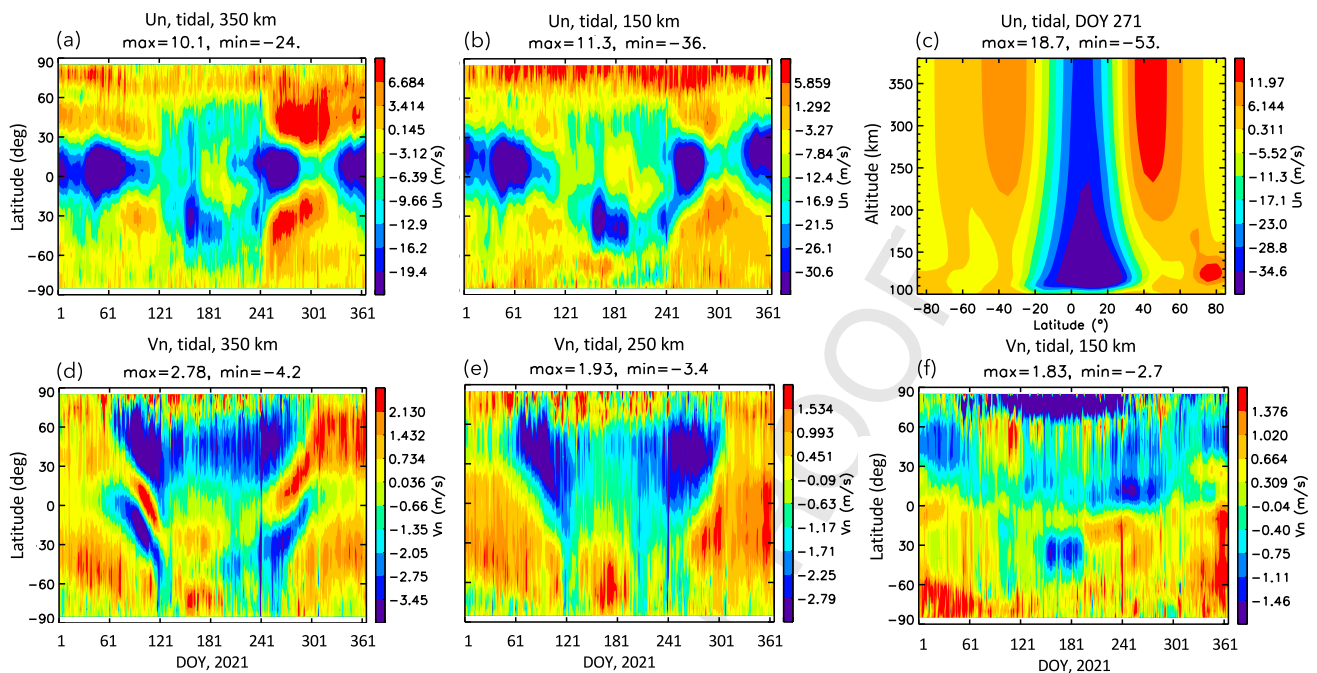


Figure 2. Depictions of tidal-forced DZM horizontal winds. (a) latvsdoy, Un, 350 km. (b) latvsdoy, Un, 150 km. (c) htvslat, Un, DOY 271. (d) latvsdoy, Vn, 350 km. (e) latvsdoy, Vn, 250 km. (f) latvsdoy, Vn, 150 km.

equinox periods. It is furthermore interesting that the influences of tides on the eastward DZM wind field extend from pole to pole; that is, Un up to $\sim 10 \text{ ms}^{-1}$ are generated at high latitudes, especially in the Northern Hemisphere (NH).

Figures 2d–2f are latvsdoy depictions of Vn at 350, 250, and 150 km, respectively. The magnitudes are notably smaller than the Un field, with magnitudes falling in the range of about $\pm 4 \text{ m/s}$ across all 3 altitudes. The transitions between positive and negative values of Vn with respect to latitude at a given DOY suggest the presence of vertical winds and the presence of cellular-like features in the meridional plane. And, the fact that these regions of divergence and convergence change with height and latitude suggest the presence of cellular-like features in both the lower and upper thermospheres, and in both hemispheres. To demonstrate this, some examples of htvslat structures of Vn and Wn for DOY 271 are shown in Figure 3. The distributions of Vn and Wn for SM forcing are illustrated in Figures 3a and 3c, respectively. Although no tidal forcing exists at the lower boundary of this simulation, it is quite evident that cellular-like circulations exist within the domain, and moreover those that exist at low to middle latitudes appear to have an upper-thermosphere origin. We surmise that these are the signatures of the harmonics of the diurnal wind field and the diurnal variation of ion drag combining nonlinearly to produce DZM momentum sources as shown by Dickinson et al. (1975, 1977), as well as higher-order tidal sources (e.g., Forbes & Garrett, 1979). In principle, similar mean and tidal forcing terms can arise in the thermal energy equation.

As indicated in the tidal-forced Vn and Wn fields in Figures 3b and 3d, there is a degree of anti-correlation with the SM fields in Figures 3a and 3c in the upper thermosphere at low to middle latitudes. For instance, the upwelling/downwelling regions in Figure 3c between $\pm 40^\circ$ latitude and above 250 km are replaced by downwelling/upwelling regions in Figure 3d. This means that the effect of upward-propagating tides is to diminish the influence of these sources of ion drag-wind interaction origin in the SM-forced I-T. Note also that there is a large counter-clockwise cell extending between 100 and 250 km in the NH with upwelling near the pole and downwelling near 10°S , and a weaker counter circulation over the same height range between 60°S and 10° (Figure 3d). There are also weaker circulations below $\sim 150 \text{ km}$ that do not show up on the scales depicted in this figure (however, see Figures 6a and 6b). Other notable aspects of this DOY 271 tidal-driven circulation is that the Vn and Wn attain overall maximum and minimum magnitudes of order 50% of their SM counterparts, extend from pole to pole, and encompass the whole thermosphere.

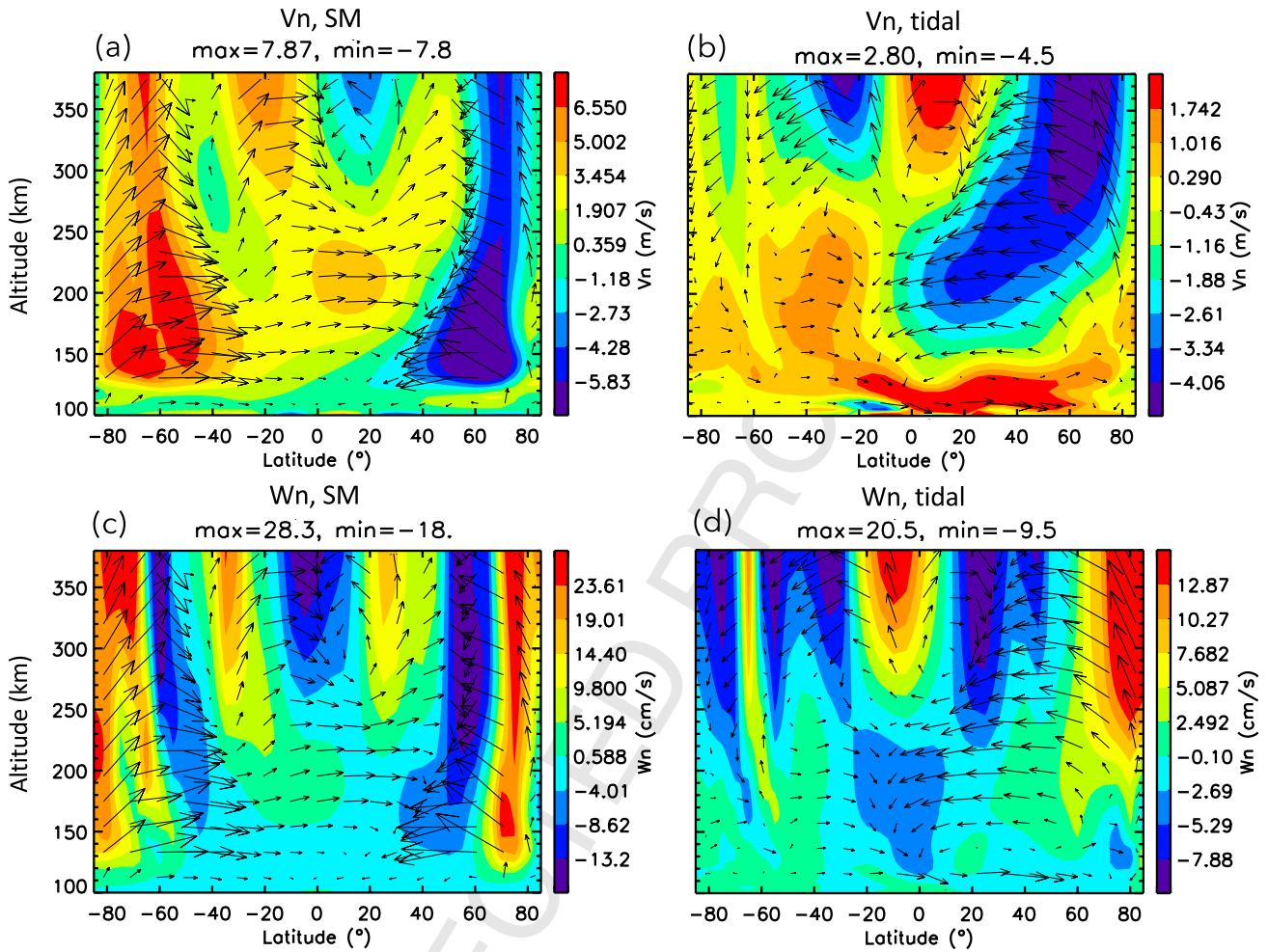


Figure 3. Htvslat depictions of Vn and Wn at DOY 271. (a) Vn, SM forcing. (b) Vn, tidal forcing. (c) Wn, SM forcing. (d) Wn, tidal forcing. The same DZM wind vectors are superimposed in (a, c) and in (b, d); Vn:Wn scaling is 1 m/s: 2 cm/s.

We now turn to the implications of these tidal-driven circulation systems on quantities of importance to space weather, such as Ne. Figure 4a illustrates the latvsday distribution of Ne at 350 km corresponding to SM + tidal forcing. Ne is mainly confined to $\pm 25^\circ$ latitude, although Ne generally maximizes during daytime and at $\pm 15\text{--}20^\circ$ magnetic latitude, that is, at the equatorial ionospheric anomaly (EIA) peaks. (At 350 km, this smearing of the EIA as a result of longitudinal averaging in geographic coordinates is particularly evident. At lower heights the EIA is visible in the DZM Ne and its variances; see, e.g., Figures 5a and 9e, and Figure 10.) The Ne SM + tidal distribution in Figure 4a is uncorrelated with the corresponding O/N₂ latvsday distribution illustrated in Figure 4d, indicating that there are other factors determining the distribution of Ne besides O/N₂. O/N₂ maximizes at middle to high latitudes in the winter hemisphere (WH), in accord with the mean summer to winter diabatic circulation indicated by the white arrows, and consistent with the accompanying (and presumed) upwelling of N₂ at middle to high latitudes in the winter hemisphere (WH).

The corresponding tidal-forced Ne and O/N₂ in Figures 4b and 4e are generally anti-correlated with those in Figures 4a and 4d, respectively. That is, the main effect of tides is to induce reductions in Ne and O/N₂ up to 30%–40% of their SM + tidal values. The reductions at DOY 271 is one such example, and its location is highlighted in all panels of Figure 4 for later reference.

The tidal-forced Tn in Figure 4c is anti-correlated with that of O/N₂ in Figure 4e. The same is true for the upward component of Wn in Figure 4f, although the region of positive correlation with O/N₂ is narrower in latitude than Tn, and furthermore is bounded at adjacent latitudes by downwelling. The upwelling region in Figure 4f could

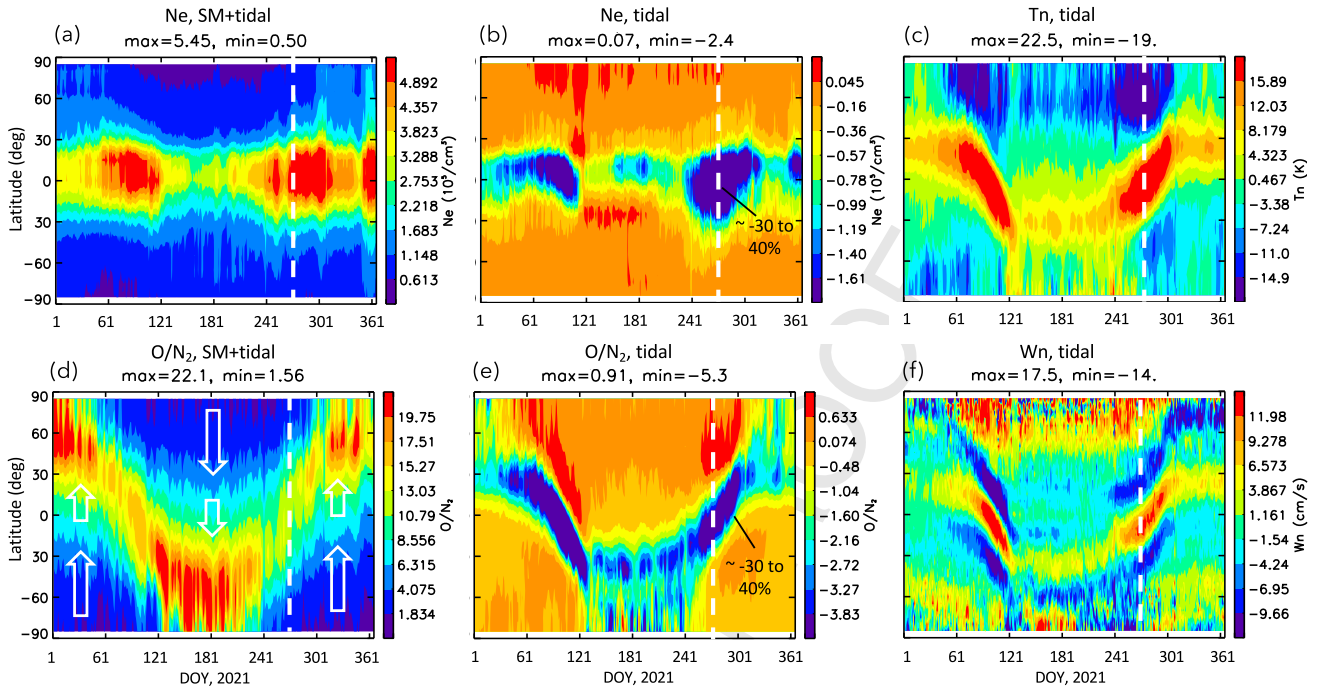


Figure 4. Latvsdoy depictions at 350 km. (a) Ne, SM + tidal forcing. (b) Ne, tidal forcing. (c) Tn, tidal forcing. (d) O/N₂, SM + tidal forcing. White arrows denote qualitative DZM solar EUV-driven circulation (see also Figure 6a). (e) O/N₂, tidal forcing. (f) Wn, forcing. White vertical dashed lines denote DOY 271.

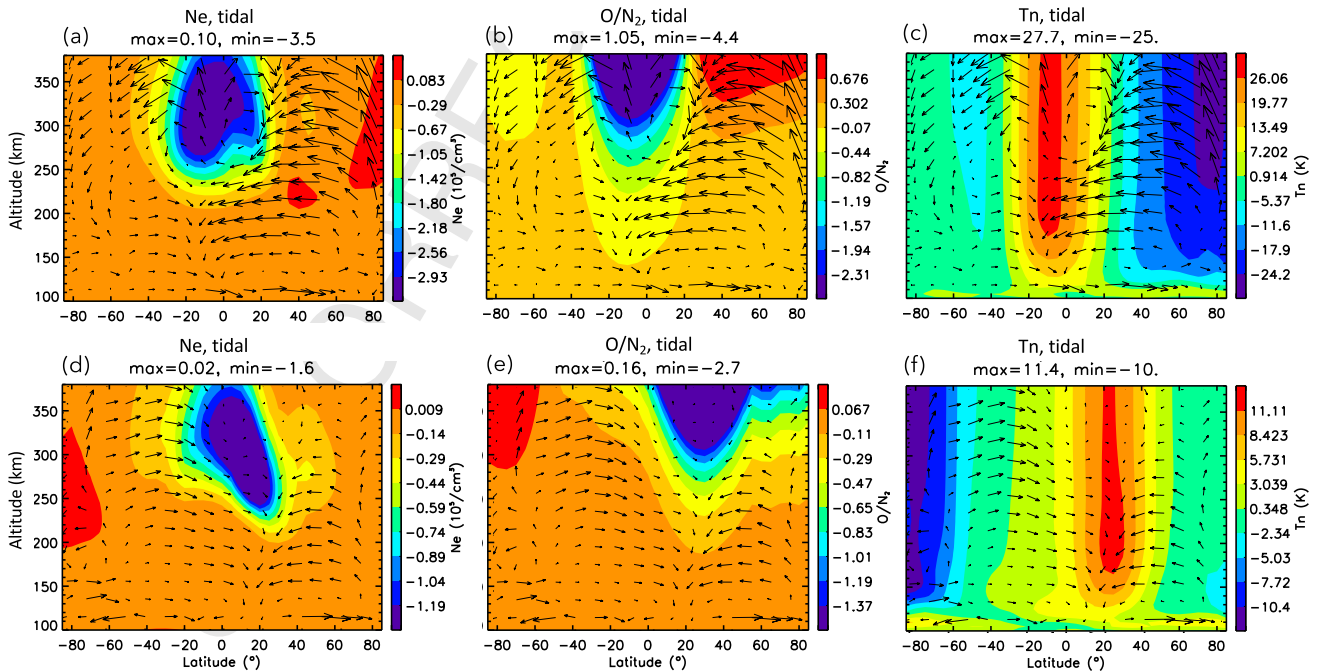


Figure 5. Htvslat depictions of DZM (a) Ne, (b) O/N₂, and (c) Tn at DOY 271, all due to tidal forcing. (d–f) Same as (a–c), except at DOY 31. The same DZM wind vectors are superimposed in (a–c) and in (d–f) Vn:Wn scaling is 1 m/s: 2 cm/s.

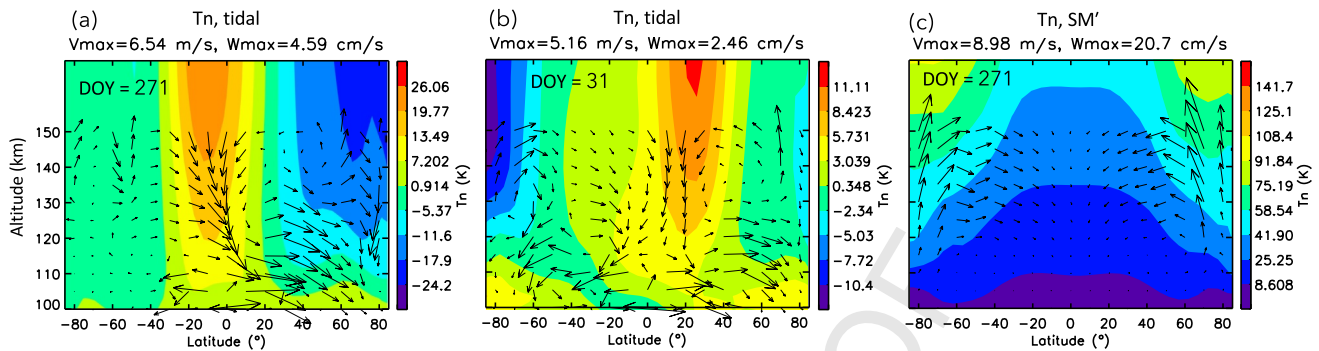


Figure 6. Htvslat depictions of T_n , 100–175 km, with DZM wind vectors superimposed 100–150 km; $V_n:W_n$ scaling is 1 m/s: 2 cm/s. (a) Tidal-forced, DOY 271. (b) Tidal-forced, DOY 31. (c) SM'-forced, DOY 271.

suggest upward transport of N_2 , which results in the reduction on O/N_2 over the same ranges of latitude and DOY. However the W_n plot in Figure 3d indicates that the equatorial upwelling does not extend below 250 km, that is, into the N_2 -rich region of the thermosphere, which casts doubt on this explanation. Although not illustrated here, the tidal-driven W_n increases considerably with height in addition to changing its latvsdoym character; at 150 and 250 km, the typical range of values for W_n over the globe are ± 3 cm/s and ± 6 cm/s, respectively.

Next, the processes determining the O/N_2 and Ne responses are pursued. Figures 5a–5c depict the htvslat structures of tidal-forced Ne, O/N_2 and T_n , respectively corresponding to the dashed white lines at DOY 271 in Figures 4b, 4c, and 4e. (Note that the Ne reductions near 300 km altitude in (a) and the htvslat temperature perturbation in (c), are similar to those of NmF2 (T_n) displayed in Figure 10 (Figure 1) at solar minimum for September in Jones et al., 2016.) Superimposed are the tidal-driven circulations illustrated in Figures 3b and 3d. Having cast doubt on the prospect that the equatorial-region reduction in O/N_2 is due to N_2 transport from below, we now pursue the alternative explanation that the observed change in O/N_2 is simply explicable in terms of the hydrostatic law and the T_n distribution in Figure 5c. This is simple to do using the hydrostatic law, knowing the scale heights of O and N_2 and the values of O/N_2 at a reference height. For DOY 271 at the equator, the DZM exosphere temperature (T_∞) from the SM'-forced calculation is 725 K and we take a mean value of the tidal-forced T_n to be 25 K, both constant with height above 150 km. The scale heights for N_2 and O are calculated to be 23.7 and 41.5 km for $T_\infty = 725$ K, and 24.5 and 42.9 K for $T_\infty = 750$ K. Taking O/N_2 values of 0.40 and 0.32, respectively, at 150 km from the model calculations (see Figure S2 in Supporting Information S1), we estimate the corresponding values at 350 km to be 14.92 and 10.61, yielding a tidal-forced value of -4.3 . This is very close to the model value of -4.2 , leading to the conclusion that the temperature effect vis-a-vis the hydrostatic law fully explains the tidal-forced perturbation in O/N_2 , at least above 150 km, which is qualitatively consistent with the resulting perturbation in Ne.

As a check on the prevalence of this interpretation, a similar calculation was performed for DOY 31, which is a more extreme case in that the T_n maximum is displaced from the equator to $+20^\circ$, and is much weaker. The sequence of htvslat plots of Ne, O/N_2 , and T_n are shown as panels (d), (e) and (f) in the bottom row of Figure 5. We see that the O/N_2 minimum is moved to $+20^\circ$ latitude in concert with T_n . Moreover, the minimum(maximum) of $O/N_2(T_n)$ are coincident with the region of downwelling near $+20^\circ$, which is opposite to what one would expect if upwelling of N_2 were to be invoked to explain the decrease in O/N_2 at higher altitudes. Using the same type of calculation performed for DOY 271, and using T_∞ values of 700 and 711 K along with O/N_2 values at 150 km of 0.38 and 0.33 (see Figure S2 in Supporting Information S1), we arrive at a tidal-forced value for O/N_2 of -3.15 at 350 km, which can be compared with the model value of -3.5 . Again, the hydrostatic law mostly explains the observed effect above 150 km; however, transport is likely the determining factor leading to the reference values of O/N_2 at 150 km used in these calculations, a conclusion drawn from Jones et al. (2016), Qian and Yue (2017), and Wang et al. (2023) and other works cited therein. Such studies that depict results in pressure coordinates emphasize the role of vertical winds, that is, departures from hydrostatic equilibrium, and generally do not mention the role of wave-driven DZM temperatures in transmitting the composition effects to higher altitudes.

Examination of all the panels in Figure 5 furthermore indicate that the height-latitude region of the most pronounced depressions in both O/N_2 and Ne, as well as maximum T_n , occur in the region of low-latitude downwelling. Figure 6 takes a closer look at the temperature structure and DZM circulation below 175 and 150 km, respectively, for (a) DOY 271 and (b) DOY 31. For both DOY, there is a convergence and downwelling above about 110 km that coincides with the maximum and in temperature. This suggests that the temperature increase is the result of adiabatic warming. In fact, many of the wind vectors are pointing downward into regions of temperature elevation and upward into regions of cooling, also suggesting the presence of adiabatic heating and cooling. As noted by Jones et al. (2016) the illustrated temperature changes are also influenced by heat flux divergences.

By way of contrast, Figure 6c illustrates the corresponding plot for SM' temperatures at DOY 271. Here the wind vectors are pointing *upward* into higher temperature regions and downward into lower temperature regions. Here the winds are *responding* to high-latitude heating as part of a thermally forced (direct) circulation, similar to the one described in the Introduction. This solar-driven DZM circulation and its variability are examined in the next section.

3.2. Meridional Circulation, O/N_2 and Ne Forced From Above

Similar to the isolation of responses to tides described in the previous subsection, results illustrated here are obtained by first taking grid point-by-grid point differences between the TIEGCM-ICON SM + tidal outputs and the corresponding outputs with conSM + tidal forcing. The conSM simulation is dominated by the seasonal-latitudinal response to constant EUV solar forcing with comparatively weak contribution from constant magnetospheric forcing and from tidal forcing. The conSM simulation is essentially a seasonal-latitudinal climatology of the I-T system. The difference fields in this case are referred to as “ SM' ”, and represent the I-T response to variable solar flux and magnetospheric forcing, consistent with similar “tidal” quantities which represent the I-T response to variable tidal forcing. Similar to SM + tidal, SM and tidal, the conSM + tidal and SM' outputs are averaged with respect to longitude and local time to obtain the DZM components of these outputs, which are used exclusively to construct the figures in this section.

While it can be expected that the I-T response to SM forcing includes some in-situ driving of the DZM circulation due to momentum sources arising from ion drag-wind nonlinear interactions, it can be safely said that the global response to SM forcing is predominantly thermally direct. This response includes vertical winds that produce adiabatic heating and cooling, constituent transport, and departures of constituents from diffusive equilibrium. Analyses of O/N_2 variability are often performed in pressure coordinates to enable isolation of the O/N_2 variability due to the vertical velocity field (e.g., Burns et al., 2015; Qian & Yue, 2017; Wang et al., 2023; Yue et al., 2019). This difference should be kept in mind when viewing the present results in the context of these previous works.

Figure 7 provides a view of the latvsdoy SM-driven variability associated with V_n and U_n . Figures 7a and 7d show V_n and U_n , respectively, for conSM + tidal forcing. These basically represent the seasonal-latitudinal climatology of the solar EUV-driven circulation, with some relatively weak contributions from constant magnetospheric forcing and variable tidal forcing. For instance, Figure 7a is dominated by summer-to-winter circulations, with weakening in the winter hemispheres (WHs), as indicated by the white arrows. To some degree equatorward flow due to high-latitude magnetospheric forcing in each hemisphere enhances the equatorward solar-driven circulation in the summer hemisphere, and weakens the meridional flow in the winter hemisphere. To first order, U_n responds to Coriolis forcing due to V_n , with U_n westward(eastward) in the summer(winter) hemisphere, with weakening of U_n following that of V_n . However, U_n does not go to zero at the equator, indicating the influence of other factors, possibly including ion drag effects and the displacement between geographic and magnetic coordinates. Close to the poles the signatures of zonal forcing, presumably due to the drag of plasma convection, becomes apparent. However, the underlying reasons for the directions of the high-latitude U_n responses in each hemisphere are not easily unraveled, as these depend on the different geometries of the driving convection patterns near the two poles, and how they respond to averaging in local time and longitude to arrive at the DZM. The salient features of the global-scale seasonal-latitudinal conSM + tidal patterns at 350 km do not differ appreciably from those at lower altitudes.

The remaining panels in this figure illustrate the SM' V_n and U_n , which are obtained by taking the DZMs of difference fields between the SM + tidal and conSM + tidal responses, which removes the responses to tidal

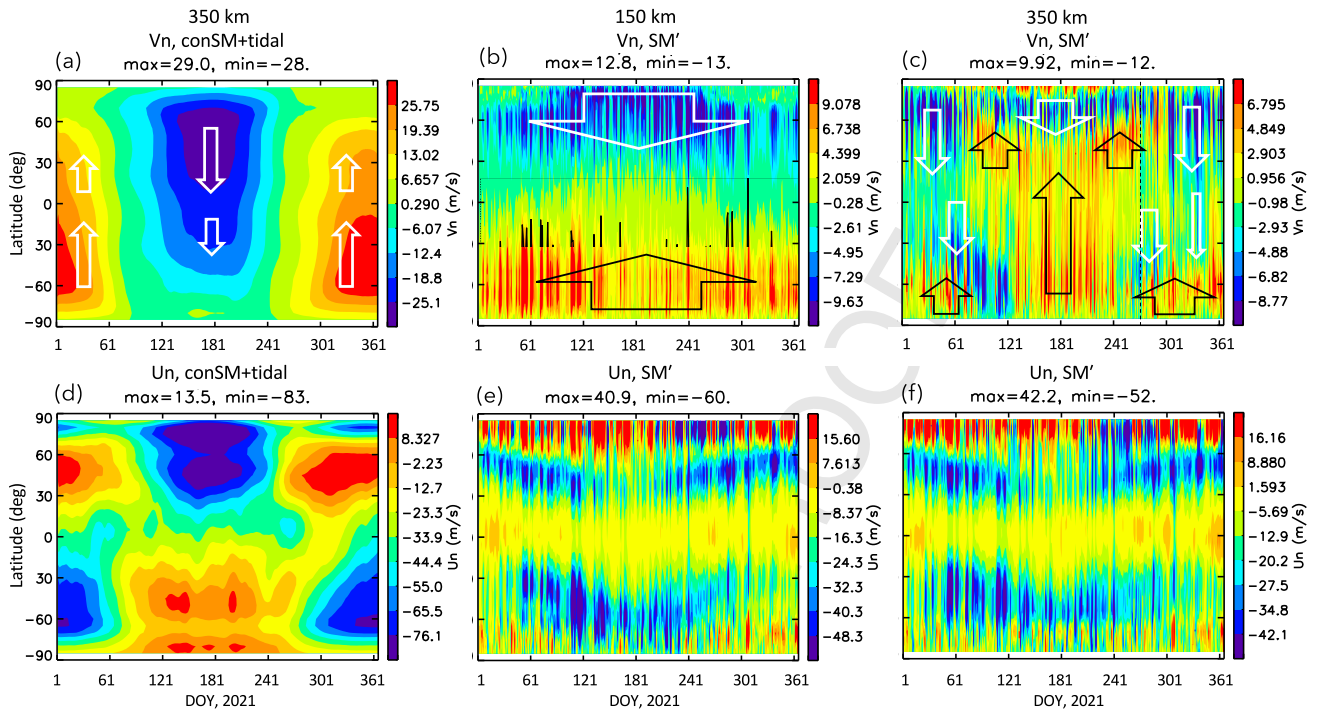


Figure 7. Latvsdoy depictions of Vn (top) and Un (bottom). (a) Vn, conSM + tidal-forced, 350 km. (b) Vn, SM'-forced, 150 km, with black vertical lines indicating CCP values ≥ 70 kV from Figure 1. (c) Vn, SM'-forced, 350 km. (d–f) same as (a–c) except for Un. The vertical dashed line in (c) indicates DOY 271.

forcing and references the SM variability (SM') against the conSM response. Figures 7b and 7e illustrate the latvsdoy variabilities of SM'-driven Vn and Un, respectively. In the aggregate, Vn at 150 km in Figure 7b is equatorward in both hemispheres, a little stronger during summer in both hemispheres, consistent with the dominance of Joule heating. Responses to daily enhancements in magnetic activity are clearly seen, as indicated by the coincidence of large spikes in Vn with vertical black lines that denote DOY with CCP ≥ 70 kV (cf. compare Figure 1.). The blue bands in SM'-driven Un in Figure 7e, combined with the near-zero values at the equator, suggest the influence Coriolis forcing. The multitude of spikes in Un magnitudes poleward of $\sim 60^\circ$ latitude in each hemisphere represent the signatures of momentum forcing by convection plasma drifts, as manifest in the DZM. The higher magnitudes in the NH may be due in part to the lower magnetic field intensity $|B|$ in the NH versus SH polar regions, since the driving convection drifts are inversely proportional to $|B|$, but the geometry as manifested in geographic coordinates must also be playing a role.

Figures 7c and 7f show the SM'-driven Vn and Un, respectively, at 350 km. For Un, there is very little difference in structure and magnitude compared to 150 km in Figure 7e. While similar magnitudes prevail at 150 and 350 km for Vn (Figure 7b vs. Figure 7c), there are distinct differences in latvsdoy structures, with regions of convergence that suggest the presence of Wn at 350 km. The latvsdoy structure of SM'-driven Wn, and an example of a corresponding circulation pattern, are considered further below. First, however, we consider the “forcing from above” complement to Figure 4 that is provided in Figure 8.

Figures 8a and 8d show the conSM results for Ne and O/N₂, respectively, at 350 km. The solid black lines in panels (b), (c), (e) and (f) represent daily F10.7 variability from Figure 1, which can be referred to for absolute values. These figures basically reflect seasonal-latitudinal climatologies of these quantities at 350 km with the effects of tidal forcing from below included. The difference fields between the outputs corresponding to Figure 4a minus 8(a) and 4(d) minus 8(d), are shown in Figures 8b and 8e, respectively. These SM' depictions represent the isolated effects of variable forcing from above; that is, departures from the seasonal-latitudinal climatologies without tidal forcing. Note that the day-to-variability reflected in Figures 8b and 8e are much more significant than the tidal-forced counterparts in Figures 4b and 4e; while the results in Figure 8 represent true variability at 1-day resolution, those in Figure 4 represent 45-day running means at 1-day resolution.

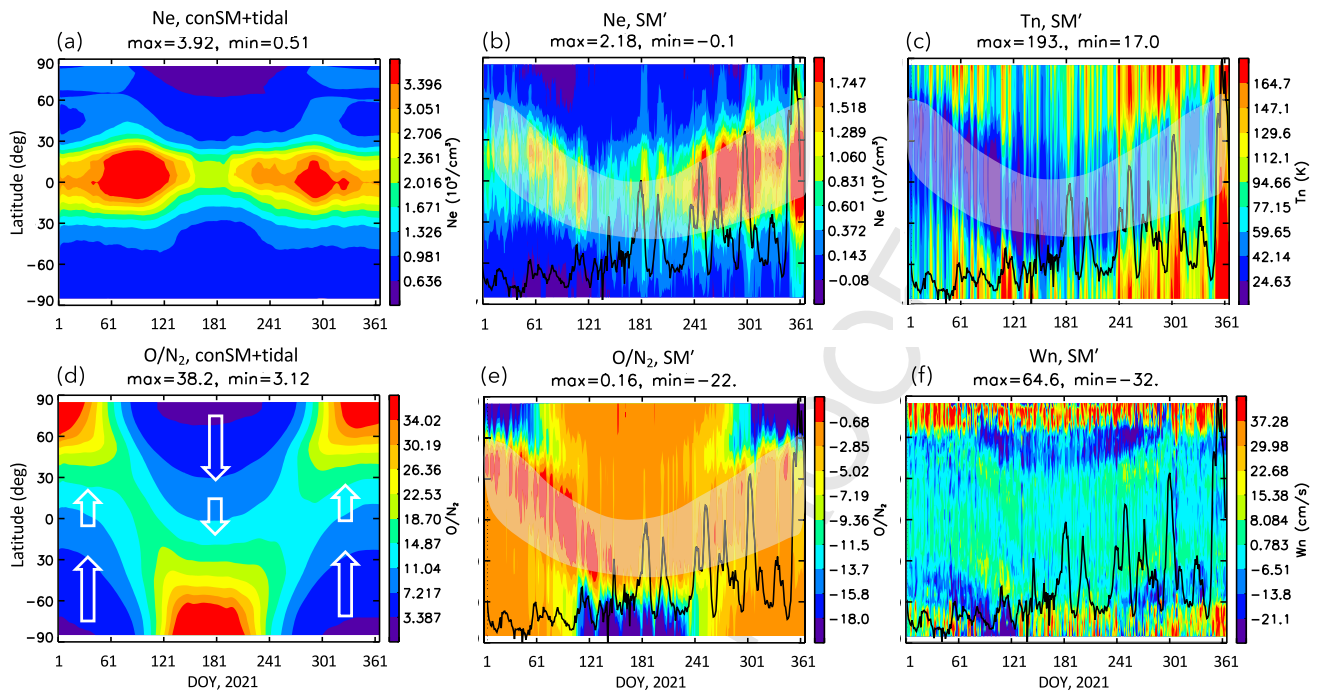


Figure 8. Latvody depictions of DZM (a) Ne, conSM + tidal-forced; (b) Ne, SM'-forced; (c) Tn, SM'-forced; (d) O/N_2 , conSM + tidal-forced, where the white arrows qualitatively indicate the solar EUV-driven circulation; (e) O/N_2 , SM'-forced; and (f) W_n , SM'-forced; at 350 km. The shaded regions in (b, c) highlight the anti-correlations of Ne and Tn with that of O/N_2 in the shaded region of (e). The solid black lines in panels (b, c, e, f) represent daily F10.7 variability from Figure 1, which can be referred to for absolute values.

Figure 8c illustrates the corresponding SM'-forced variability in Tn. Following the gray shaded area from midlatitudes in the NH at DOY 1, toward the equator and into the SH around DOY 181, and then back into NH midlatitudes, we see generally lower values of Tn prior to DOY 181 and progressively larger Tn thereafter. This is broadly consistent with the upward trend of F10.7 throughout the year, reflecting the connection between Tn and EUV heating. The Tn responses to enhancements in F10.7 associated with the solar rotation effect are also very clear throughout the year. Interestingly, the largest Tn enhancements associated with F10.7 are at high latitudes in each hemisphere, which suggests that solar-induced enhancements in conductivity may in turn be boosting Joule heating rates. In fact, there is some suggestive evidence for correlations between peaks in Tn and peaks in CCP, but they are difficult to separate from the influences of solar flux, which tends to be enhanced within the same active regions that spawn the origins of magnetic activity.

In Figure 8e an anti-correlation between O/N_2 and Tn exists before and after DOY 181, as would be expected from the hydrostatic law. However, an increase(decrease) in O/N_2 before(after) DOY 181 along the shaded region does not translate to Ne in Figure 8b, which in fact indicates smaller(larger) Ne densities before(after) DOY 181. This is simply due to the fact that EUV production of Ne is greater after DOY 181, as is evident from the general upward trend of F10.7 as well as the enhancements in Ne in connection with the solar rotation effect; the effect of increased solar flux simply outweighs the decrease in O/N_2 .

The latvody depiction of W_n at 350 km is shown in Figure 8f. Similar to the tidal-driven W_n , the global ranges of SM'-forced W_n increase with height from -5 to $+20$ cm/s at 150 km and -15 to $+30$ cm/s at 250 km (not shown), to roughly -25 to $+50$ cm/s at 350 km. A distinctive feature of Figure 8f (and those for other heights) is the much greater tendency for upwelling poleward of $65^\circ N$ as compared with the SH, where periods of downwelling occur much more frequently polewards of $60^\circ S$. In the NH between DOY 91 and 271, the high-latitude upwelling shifts to downwelling around $60^\circ N$ (as indicated by the dark blue area), and then at lower latitudes (as low as 30 – $35^\circ N$ between DOY 121–241) shifts to weaker upwelling. Referring back to Figure 7c, it is evident that these changes in W_n are connected with the latitudes of convergence of V_n , as indicated by the arrows centered on DOY 181. Similar effects are occurring during non-summer months, but the periods of downwelling are weaker and more

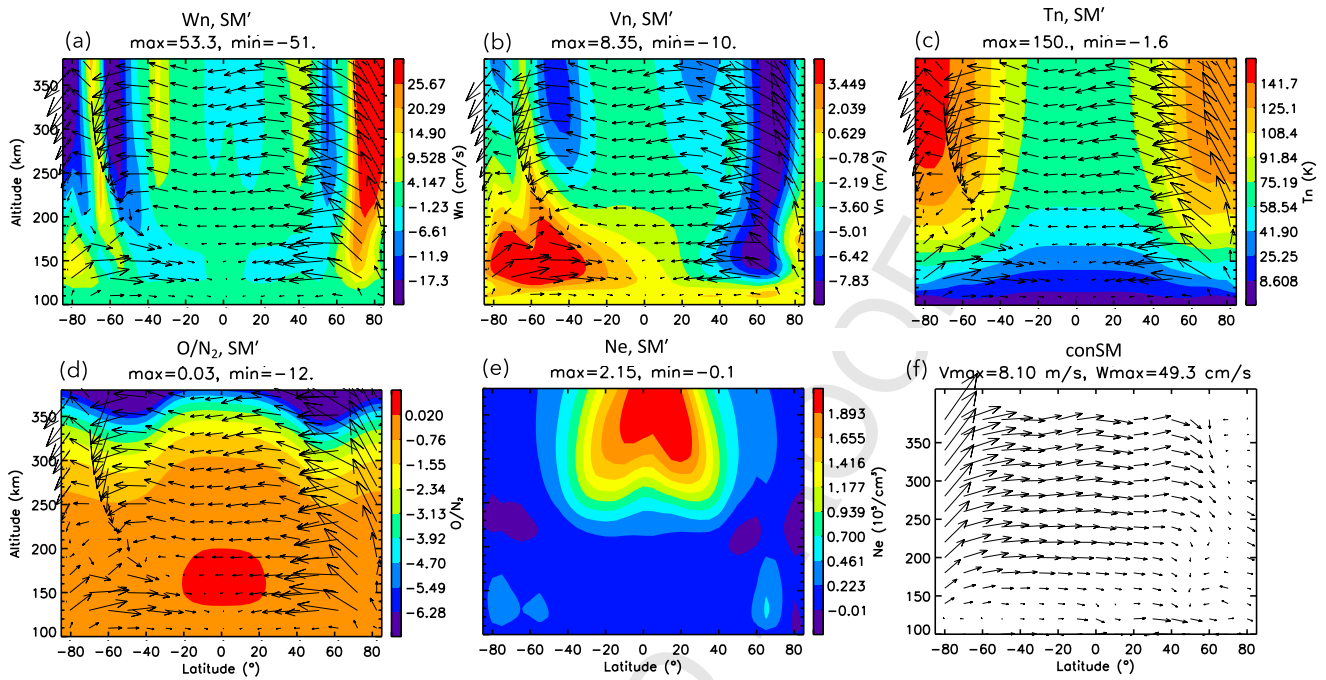


Figure 9. Htvslat depictions of SM'-forced (a) W_n , (b) V_n , (c) T_n , (d) O/N_2 and (e) Ne for DOY 271. DOY 271 is just after the equinox transition. The corresponding summer-to-winter conSM-driven DZM circulation is depicted in (f). DZM wind vectors for DOY 271 are also depicted in (a–d, f). $V_n:W_n$ scaling is 1 m/s: 2 cm/s.

infrequent. Similar shifts in the direction of W_n between the pole and low latitudes are seen during non-winter months in the SH, but the patterns are not as ordered or as strong as in the NH. This is apparently due in part to the weaker upwelling occurring at the highest latitudes in the SH as opposed to the NH. The fact that there is any seasonal-latitudinal variability in what appears to be the circulations forced by high-latitude Joule heating suggests modulation by the solar EUV-driven meridional circulation as depicted in Figure 7a. In any case, the above shifts in direction of W_n and connections with V_n suggest the presence of cellular-like circulation patterns in the thermosphere.

Figure 9 depicts these cellular-like features in the htvslat plane, comparing SM'-forced (a) W_n , (b) V_n , and (c) T_n for DOY 271, which is characterized by $F_{10.7} = 89.7$ sfu and $CCP = 56.4$ kV, not far from their respective median values of 76.9 and 49.2 during 2021. Following the wind vectors and W_n in (a), in the NH above 250 km, there are rising and equatorward motions near the pole, a degree of downwelling near 60°N and then upwelling near 40°N, and weak downwelling near the equator, which fits with the general pattern of NH behavior in Figure 8f. However, below 225 km the pattern is simpler, with just upwelling poleward of about 60°N, and equatorward motion from pole to the equator. Referring to our interpretation regarding the origin of similar high-altitude structures in W_n and V_n in connection with Figure 3, it is also surmised here that the undulations (as opposed to “cellular-like features”) in the generally southward flow at the higher altitudes are generated in-situ by momentum sources due to ion drag-neutral wind nonlinear interactions (e.g., see Dickinson et al., 1975, 1977; Forbes & Garrett, 1979). Below 175 km in the SH, the same sort of direct high-to-low latitude connection also exists (see also Figure 6c). However, at higher altitudes in the SH there are regions of downwelling near 60–70°S and poleward of 80°S that converge with the upwelling below 150 km, and feed into the equatorward flow below 175 km that eventually converges with the equatorward flow from the NH, which combine to produce downwelling near the equator (see also Figure 6c).

An interesting facet of the SM'-driven circulation is that the NH-to-SH cross-equatorial flow opposes the conSM circulation shown in Figure 9f, which mainly reflects the solar EUV-driven circulation as discussed in connection with Figure 7a. Note that DOY 271 is post-equinox transition in character with summer-to-winter DZM circulation extending from the SH into the NH, as shown in Figure 9f. The direction of the SM' inter-hemispheric flow above ~200 km must be due to some inter-hemispheric asymmetry in magnetospheric energy inputs above

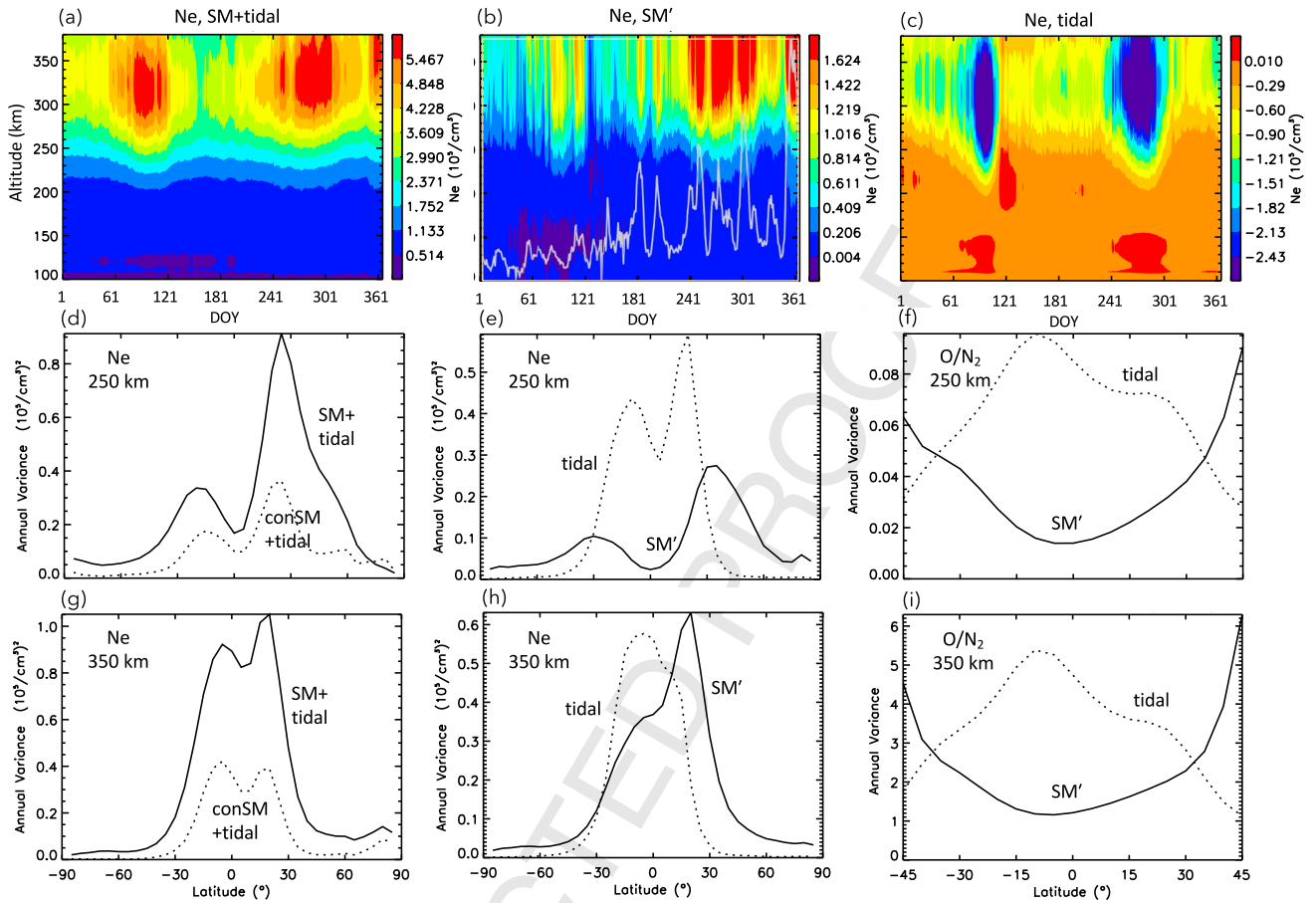


Figure 10. Top row: htsvdoys depictions of Ne at the equator: (a) SM + tidal-forced. (b) SM'-forced. (c) Tidal-forced. In (b) the daily F10.7 fluxes are overlaid to illustrate the correlation with Ne. Middle row: Annual variances as a function of latitude at 250 km. (d) Ne, SM + tidal- and conSM + tidal-forced. (e) Ne, tidal- and SM'-forced. (f) O/N₂, tidal- and SM'-forced. Bottom row: (g–i) same as (d–f) except at 350 km.

150 km, since the pole-to-pole temperature distribution and meridional circulation are symmetric about the equator below 150 km (see Figure 6c). At first sight this appears to be contradictory to the differing polar-region Tn's in Figure 9c, which we therefore conclude exist due to adiabatic heating(cooling) due to downwelling(up-welling) in the SH(NH).

Finally, we note that the latitudinal distribution of the O/N₂ ratio above 200 km in Figure 9d is consistent with that of Tn in Figure (c) and the hydrostatic law, analogous to the situation encountered with the tidal-driven circulations as displayed in Figure 5. That is, higher temperatures and larger scale heights produce larger depressions in O/N₂ ratio. However, in contrast to Figure 5, in the case of the SM'-driven circulation these O/N₂ depressions are insufficient to reduce electron densities. Instead, as shown in Figure 9e, Ne actually increases due to solar production associated with the elevated solar fluxes on DOY 271, which overcompensates for the O/N₂ effect.

3.3. Quantitative Comparisons of Responses Due To Forcing From Above and From Below

In this section we quantify the relative contributions due to forcing from above and below to the global-scale DZM circulation and corresponding DZM O/N₂ and Ne responses. This was done by computing variances in Un, Vn, Wn, Tn, O/N₂ and Ne with respect to their day-to-day variability at each latitudinal grid point at 150, 250, and 350 km. It was found that in all cases variances associated with SM' forcing far exceeded variances due to tidal forcing poleward of about ±60° latitude. And, at lower latitudes, the only tidal-forced variables that possessed variances that exceeded those of SM'-forced variables were Un at all 3 heights, Wn at 350 km, and Ne and O/N₂ at 250 and 350 km. There is evidence to suggest that Un and Wn at low latitudes play an important role in defining conditions for Rayleigh-Taylor instability and the formation of plasma bubbles in the low-latitude F-

region (e.g., Huba, 2022; Sekar et al., 1994; Shinagawa et al., 2018), underscoring the potential relevance of tidal-driven DZM winds to space weather. Ne is also of utmost importance to space weather, and the relative roles tidal-driven and SM'-driven Ne variability is the emphasis here.

The htsvdo plots of (a) SM + tidal-forced, (b) SM'-forced and (c) tidal-forced Ne at the geographic equator, the location of maximum DZM Ne (cf. Figure 4a), are provided in Figure 10. The Ne responses are seen to extend from roughly 250 km to well over 400 km, so annual variances of the daily Ne and O/N₂ responses are presented in Figures 10d–10i at the representative heights of 250 and 350 km, respectively. Figures 10d and 10g in the left column compare the variances associated with SM + tidal and conSM + tidal forcing at these two heights. SM + tidal represents the full variability of the I-T system due to forcing from both above and below. The conSM + tidal curves represent the seasonal-latitudinal solar EUV-driven climatology due to the tilt of Earth's axis with respect to the ecliptic plane, plus the variability induced by the upward-propagating tidal spectrum. In Figures 10e and 10h, the SM' curves represent the annual variances associated with day-to-day differences from the seasonal-latitudinal solar EUV-driven variability, without the effects of tides, and the dotted curves represent the day-to-day variability associated with the tides themselves. At 250 km (Figure 10e) Ne daily “weather” far exceeds that of SM', whereas at 350 km (Figure 10h) tidal- and SM'-induced Ne weather are of similar magnitude. And, all of the effects depicted in Figures 10e and 10h are confined within low to middle latitudes.

In Figures 10f and 10i the variances due day-to-day variability of O/N₂ at 250 and 350 km are illustrated. The variability due to tides exceeds that due to SM' forcing within $\pm 30^\circ$ latitude at 250 and 350 km, which mainly accounts for the results in Figures 10e and 10h, respectively. Poleward of about $\pm 45^\circ$ latitude, SM'-forced variability of O/N₂ far exceeds that due to tides, but has little impact on the SM' variability of Ne at these latitudes (Figures 10e and 10h).

4. Summary and Conclusions

In this paper we have utilized 3 specifically designed thermosphere-ionosphere general circulation model simulations to separate the DZM I-T variability driven by tides propagating up from the lower atmosphere (“tidal”) from those driven by solar flux and magnetospheric forcing combined (SM'). The focus is on eastward (Un), northward (Vn), vertical (Wn) winds and temperatures (Tn), O/N₂ density ratio, and electron density (Ne) during 2021, a year of low to moderate solar activity. Notably, the model simulations employ actual observations to define external forcing of the model: wind and temperature measurements from the ICON mission to define the tidal spectrum; measurements of solar wind magnetic fields, velocity and pressure to constrain the high-latitude energy inputs; and F10.7 variability to define the day-to-day variability in solar EUV flux. The region of study is pole-to-pole and 100–400 km, and the analysis is performed in height and geographic coordinates.

The main conclusions are summarized as follows:

1. The tidal- and SM' circulation systems both extend from pole-to-pole, and consist of open and closed cellular-like features at regional and global scales in the lower and upper thermosphere. In the upper thermosphere these cellular-like features likely arise due to momentum forcing produced by the nonlinear interaction between diurnally varying neutral winds and diurnally varying ion drag (Dickinson et al., 1975, 1977). While the characters of these circulation systems change considerably within the I-T domain, the Vn are comparable over its altitude extent. For the global tidal-driven circulation, Vn generally fall in the range of ± 2 –3 m/s, as compared with ± 9 m/s for the SM'-driven circulation. However, the Wn increase with height, falling in the ranges ± 3 , ± 6 , ± 10 cm/s at, for example, 150, 250, 350 km for the tidal-driven circulations; and -5 to $+20$ cm/s, -15 to $+30$ cm/s, and -20 to $+40$ cm/s, respectively for the SM' driven circulations. The relatively larger positive values for the SM'-driven circulation reflect upwelling due to high-latitude heating.
2. The above wind magnitudes can be compared with the Vn, Wn associated with the total SM + tidal-driven I-T circulation system: ± 20 m/s, -10 to $+40$ cm/s at 150 km; ± 25 m/s, -22 to $+80$ cm/s at 250 km; and ± 26 m/s, -30 to $+100$ cm/s at 350 km.
3. The tidal- and SM'-driven responses also consist of a DZM zonal wind field, Un. For the tidal-driven Un, responses range between -30 m/s to $+6$ m/s, without much change in magnitude or latvsdoy structure with height. The large negative values fall mainly within $\pm 30^\circ$ latitude, and appear to mainly arise from dissipation of DW1 with secondary contributions from SW2. Magnitudes and latvsdoy structures of the SM'-forced Un do not vary much either, and range in magnitude between about -50 m/s and $+30$ m/s. The largest positive Un occur at latitudes poleward of $\pm 60^\circ$ latitude, and likely arise from momentum forcing by convection-driven

- drifts. The large westward Un driven by SM' forcing occur in bands at middle to high latitudes in both hemispheres, and are largely connected with equatorward Vn vis-a-vis the Coriolis force.
4. Below ~150 km, the SM'-driven circulation is consistently characterized by upwelling at the poles, equatorward flows in each hemisphere, and downwelling at lower latitudes, consistent with driving by Joule heating. However, in the upper thermosphere the picture is less straightforward. Equatorward of $\pm 60^\circ$ latitude there are regions up upwelling and downwelling and perturbations of the meridional flows that are consistent with the presence of F-region momentum sources likely associated with neutral wind-ion drag coupling. For the illustrated example corresponding to DOY 271, inter-hemispheric flow at all altitudes exists that is counter to the summer-to-winter climatological flow due mainly to solar EUV heating. However, the day-to-day variability of these characteristics is large.
 5. In terms of annual variances associated with daily DZM fields as a function of latitude, SM'-forced variances in Un, Vn and Wn far exceed those due to tidal forcing poleward of about $\pm 60^\circ$ latitude. At lower latitudes, the only tidal-forced wind variances that exceeded the SM'-forced ones were Un at all 3 heights and Wn at 350 km. Notably, these fields are of space weather relevance, since Un and Wn at low latitudes are thought to play an important role in defining conditions for Rayleigh-Taylor instability and the formation of plasma bubbles in the low-latitude F-region (e.g., Huba, 2022; Sekar et al., 1994; Shinagawa et al., 2018).
 6. Another consequence of dissipation of the vertically propagating tidal spectrum is the production of 10–30K temperature increases within $\pm 30^\circ$ latitude, often coincident with downwelling and thus presumably a result of subsidence heating. The corresponding O/N₂ decreases at altitudes above 150 km are shown to be consistent with the hydrostatic law and these temperature increases, accounting for up to 30%–40% decreases in Ne in the F-region. Based on previous works (e.g., Jones et al., 2016; Qian & Yue, 2017; Wang et al., 2023; and references cited therein) transport likely determines the O/N₂ boundary conditions that the present hydrostatic calculations were based upon.
 7. The tidal-driven results describe above are consistent with results presented in Jones et al. (2014, 2016, 2019) for the more limited election of months, heights, latitudes, etc. considered by those authors. We surmise from this level of agreement that the results presented here are mainly driven by DW1, SW2 and DE3, and not sensitive to the differences in detail between the tides occurring during 2021 by the ICON mission, and the climatological tides derived from measurements made between 2002 and 2008 during the TIMED mission as embodied in the CTMT (Oberheide et al., 2011).
 8. In an average sense, the low to middle latitude SM'-driven Tn response as a function of DOY in the upper thermosphere is visibly anti-correlated with that of O/N₂, consistent with a hydrostatic relationship. However, SM'-driven O/N₂ are also anti-correlated with SM'-driven Ne, unlike the situation described above for the tidal-driven circulation. This is simply due to the fact the Ne variation is more responsive to the solar flux variation occurring during 2021 than to O/N₂ variability.
 9. The above conclusion is also reflected in annual variances within about $\pm 45^\circ$ ($\pm 30^\circ$) latitude, where tidal-driven DZM Ne(O/N₂) variances exceed or equal those of the SM-driven variances.

While day-to-day variability is the minimum and natural time resolution for considering variability of DZM quantities, one caveat to the above results and conclusions is that the day-to-day variability due to tidal forcing from below corresponds to variability with respect to 45-day running means, whereas the response due to forcing from above corresponds to true day-to-day variability. The 45-day windows are necessitated by the local time precession of the ICON satellite, a shortcoming universally encountered in single-satellite missions. A second caveat is that the forcing from below does not consider the effects of gravity waves (GWs), both in terms of the variability that they exert directly on the I-T, but also on the tidal forcing due to GW-tide interactions. Thus the contributions from below in the present study are underrepresented, and may be viewed as a lower limit. The Atmospheric Waves Experiment (AWE) launched to the International Space Station on 22 November 2023, and now successfully acquiring data, represents a first step toward ameliorating these shortcomings. AWE is expected to characterize the GW spectrum entering the I-T at the mesopause (~87 km) over 85% of the globe every 4 days for a period of at least 2 years, and should make possible the first observation-based estimates of the impacts GWs on the global I-T. Within the next decade, the expectation is that the multi-satellite DYNAMIC mission will measure tidal and DZM variability concurrent with in-situ I-T measurements by the multi-satellite GDC mission over most of the globe at a cadence of a few days, thus enabling characterization and comparisons of the I-T response due to forcing from above and from below on an equal footing. Until that time, the present work provides a first interim look at DZM I-T variability driven from above and below.

Data Availability Statement

The TIEGCM-ICON data analyzed here are available from Maute and Zhang (2024).

Acknowledgments

ICON is supported by NASA's Explorers Program through contracts NNG12FA45C and NNG12FA42I. AM was supported by NASA ICON Grant 80NSSC23K1123 and previous ICON Grant 80NSSC21K1990.

References

- Andrews, D. G., Holton, J. R., & Leovy, C. B. (1987). Middle atmosphere dynamics. In *International geophysics series* (Vol. 40). Academic press. xi + 489. ISBN: 9780120585762.
- Angelats i Coll, M., & Forbes, J. M. (2002). Nonlinear interactions in the upper atmosphere: The $s = 1$ and $s = 3$ nonmigrating semidiurnal tides. *Journal of Geophysical Research*, 107(A8), 1157. <https://doi.org/10.1029/2001JA900179>
- Burns, A. G., Solomon, S. C., Wang, W., Qian, L., Zhang, Y., Paxton, L. J., et al. (2015). Explaining solar cycle effects on composition as it relates to the winter anomaly. *Journal of Geophysical Research: Space Physics*, 120(7), 5890–5898. <https://doi.org/10.1002/2015JA021220>
- Cullens, C. Y., Immel, T. J., Triplett, C. C., Wu, Y. J., England, S. L., Forbes, J. M., & Liu, G. (2020). Sensitivity study for ICON tidal analysis. *Progress in Earth and Planetary Science*, 7(1), 18. <https://doi.org/10.1186/s40645-020-00330-6>
- Dickinson, R. E., Ridley, E. C., & Roble, R. G. (1975). Meridional circulation in the thermosphere I. Equinox conditions. *Journal of the Atmospheric Sciences*, 32(9), 1737–1754. [https://doi.org/10.1175/1520-0469\(1975\)032<1737:MCITTI>2.0.CO;2](https://doi.org/10.1175/1520-0469(1975)032<1737:MCITTI>2.0.CO;2)
- Dickinson, R. E., Ridley, E. C., & Roble, R. G. (1977). Meridional circulation in the thermosphere. II. Solstice conditions. *Journal of the Atmospheric Sciences*, 34(1), 178–192. [https://doi.org/10.1175/1520-0469\(1977\)034<0178:MCITTI>2.0.CO;2](https://doi.org/10.1175/1520-0469(1977)034<0178:MCITTI>2.0.CO;2)
- Emery, B., Roble, R., Ridley, E., Richmond, A., Knipp, D., Crowley, G., et al. (2012). *Parameterization of the ion convection and the auroral oval in the NCAR thermospheric general circulation models. Technical Note NCAR/TN-491+STR*. University Corporation for Atmospheric Research. <https://doi.org/10.5065/D6N29TXZ>
- Forbes, J. M., & Garrett, H. B. (1979). Theoretical studies of atmospheric tides. *Reviews of Geophysics*, 17(8), 1951–1981. <https://doi.org/10.1029/RG017i008p01951>
- Forbes, J. M., Roble, R. G., & Fesen, C. G. (1993). Acceleration, heating, and compositional mixing of the thermosphere due to upward propagating tides. *Journal of Geophysical Research*, 98(A1), 311–321. <https://doi.org/10.1029/92JA00442>
- Forbes, J. M., & Zhang, X. (2022). Hough mode extensions (HMEs) and solar tide behavior in the dissipative thermosphere. *Journal of Geophysical Research: Space Physics*, 127(11), e2022JA030962. <https://doi.org/10.1029/2022JA030962>
- Forbes, J. M., Zhang, X., Hagan, M. E., England, S. L., Liu, G., & Gasperini, F. (2017). On the specification of upward-propagating tides for ICON science investigations. *Space Science Reviews*, 212(1–2), 697–713. <https://doi.org/10.1007/s11214-017-0401-5>
- Forbes, J. M., Zhang, X., Palo, S., Russell, J., Mertens, C. J., & Mlynczak, M. (2008). Tidal variability in the ionospheric dynamo region. *Journal of Geophysical Research*, 113(A2), A02310. <https://doi.org/10.1029/2007JA012737>
- Forbes, J. M., Zhang, X., Talaat, E. R., & Ward, W. (2003). Nonmigrating diurnal tides in the thermosphere. *Journal of Geophysical Research*, 108(A1), 1033. <https://doi.org/10.1029/2002JA009262>
- Holton, J. R. (1983). The influence of gravity wave breaking on the general circulation of the middle atmosphere. *Journal of the Atmospheric Sciences*, 40(10), 2497–2507. [https://doi.org/10.1175/1520-0469\(1983\)040<2497:TIOGWB>2.0.CO;2](https://doi.org/10.1175/1520-0469(1983)040<2497:TIOGWB>2.0.CO;2)
- Huba, J. D. (2022). Generalized Rayleigh-Taylor instability: Ion inertia, acceleration forces, and E region drivers. *Journal of Geophysical Research: Space Physics*, 127(6), e2022JA030474. <https://doi.org/10.1029/2022JA030474>
- James, I. N. (2002). Hadley circulation. In J. R. Holton, J. A. Curry, & J. A. Pyle (Eds.), *Encyclopedia of atmospheric sciences* (1st ed., pp. 919–924). Academic Press. ISBN 9780122270901. <https://doi.org/10.1016/B0-12-227090-8/00161-5>
- Jones, M., Jr., Forbes, J. M., & Hagan, M. E. (2016). Solar cycle variability in mean thermospheric composition and temperature induced by atmospheric tides. *Journal of Geophysical Research: Space Physics*, 121(6), 5837–5855. <https://doi.org/10.1002/2016JA022701>
- Jones, M., Jr., Forbes, J. M., Hagan, M. E., & Maute, A. (2014). Impacts of vertically propagating tides on the mean state of the ionosphere-thermosphere system. *Journal of Geophysical Research: Space Physics*, 119(3), 2197–2213. <https://doi.org/10.1002/2013JA019744>
- Jones, M., Jr., Forbes, J. M., & Sassi, F. (2019). The effects of vertically propagating tides on the mean dynamical structure of the lower thermosphere. *Journal of Geophysical Research: Space Physics*, 124(8), 7202–7219. <https://doi.org/10.1029/2019JA026934>
- Lindzen, R. S. (1981). Turbulence and stress owing to gravity wave and tidal breakdown. *Journal of Geophysical Research*, 86(C10), 9707–9714. <https://doi.org/10.1029/JC086iC10p09707>
- Maute, A. (2017). Thermosphere-ionosphere-electrodynamics general circulation model for the ionospheric connection explorer: TIEGCM-ICON. *Space Science Reviews*, 212(1–2), 523–551. <https://doi.org/10.1007/s11214-017-0330-3>
- Maute, A., Forbes, J. M., Cullens, C. Y., & Immel, T. J. (2023). Delineating the effect of upward propagating migrating solar tides with the TIEGCM-ICON. *Frontiers in Astronomical and Space Sciences*, 10, 1–15. <https://doi.org/10.3389/fspas.2023.1147571>
- Maute, A., & Zhang, X. (2024). TIEGCM zonal and diurnal mean data set for 2021 with LB tides, without LB tides, with constant solar forcing [Dataset]. *Zenodo*. <https://doi.org/10.5281/zenodo.10484430>
- Miyahara, S. (1978). Zonal mean winds induced by vertically propagating atmospheric tidal waves in the lower thermosphere, part II. *Journal of the Meteorological Society of Japan*, 56(6), 548–558. https://doi.org/10.2151/jmsj1965.56.6_548
- Miyahara, S., & Wu, D. (1989). Effects of solar tides on the zonal mean circulation in the lower thermosphere: Solstice condition. *Journal of Atmospheric and Solar-Terrestrial Physics*, 51(7–8), 635–647. [https://doi.org/10.1016/0021-9169\(89\)90062-7](https://doi.org/10.1016/0021-9169(89)90062-7)
- Miyoshi, Y., & Yigit, E. (2019). Impact of gravity wave drag on the thermospheric circulation: Implementation of a nonlinear gravity wave parameterization in a whole-atmosphere model. *Annales Geophysicae*, 37(5), 955–969. <https://doi.org/10.5194/angeo-37-955-2019>
- Oberheide, J., Forbes, J. M., Zhang, X., & Bruinsma, S. L. (2011). Climatology of upward propagating diurnal and semidiurnal tides in the thermosphere. *Journal of Geophysical Research*, 116(A11), A11306. <https://doi.org/10.1029/2011JA016784>
- Qian, L., Burns, A., Emery, B. A., Foster, B. T., Lu, G., Maute, A., et al. (2014). In J. Huba, R. Schunk, & G. Khazanov (Eds.), *The NCAR TIEGCM: A community model of the coupled thermosphere/ionosphere system. Modeling the ionosphere-thermosphere system* (pp. 73–84). John Wiley & Sons. <https://doi.org/10.1002/9781118704417.ch7>
- Qian, L., Burns, A., & Jia, Y. (2017). Evidence of the lower thermospheric winter-to-summer circulation from SABER CO₂ observations. *Geophysical Research Letters*, 44(20), 10100–10107. <https://doi.org/10.1002/2017GL075643>
- Qian, L., & Yue, J. (2017). Impact of the lower thermospheric winter-to-summer residual circulation on thermospheric composition. *Geophysical Research Letters*, 44(9), 3971–3979. <https://doi.org/10.1002/2017GL073361>
- Richards, P. G., Fennelly, J. A., & Torr, D. G. (1994). EUVAC: A solar EUV flux model for aeronomic calculations. *Journal of Geophysical Research*, 99(A5), 8981–8992. <https://doi.org/10.1029/94JA00518>

- Richmond, A. (1995). Ionospheric electrodynamics using magnetic apex coordinates. *Journal of Geomagnetism and Geoelectricity*, 47(2), 191–212. <https://doi.org/10.5636/jgg.47.191>
- Roble, R., & Ridley, E. (1987). An auroral model for the NCAR thermospheric general circulation model (TGCM). *Annales Geophysicae - Series A: Upper Atmosphere and Space Sciences*, 5, 369–382.
- Sekar, R., Suhasini, R., & Raghavarao, R. (1994). Effects of vertical winds and electric fields in the nonlinear evolution of equatorial spread F. *Journal of Geophysical Research*, 99(A2), 2205–2213. <https://doi.org/10.1029/93JA01849>
- Shinagawa, H., Jin, H., Miyoshi, Y., Fujiwara, H., Yokoyama, T., & Otsuka, Y. (2018). Daily and seasonal variations in the linear growth rate of the Rayleigh-Taylor instability in the ionosphere obtained with GAIA. *Progress in Earth and Planetary Science*, 5(1), 16. <https://doi.org/10.1186/s40645-018-0175-8>
- Truskowski, A. O., Forbes, J. M., Zhang, X., & Palo, S. E. (2014). New perspectives on thermosphere tides: 1. Lower thermosphere spectra and seasonal-latitude structures. *Earth Planets and Space*, 66, 1–17. <https://doi.org/10.1186/s40623-014-0136-4>
- Wang, J. C., Yue, J., Wang, W., Qian, L., Jones, M., Jr., & Wang, N. (2023). The lower thermospheric winter-to-summer meridional circulation: 2. Impact on atomic oxygen. *Journal of Geophysical Research: Space Physics*, 128(11), e2023JA031684. <https://doi.org/10.1029/2023JA031684>
- Wang, J. C., Yue, J., Wang, W., Qian, L., Wu, Q., & Wang, N. (2022). The lower thermospheric winter-to-summer meridional circulation: 1. Driving mechanism. *Journal of Geophysical Research: Space Physics*, 127(12), e2022JA030948. <https://doi.org/10.1029/2022JA030948>
- Wang, N., Qian, L., Yue, J., Wang, W., Mlynczak, M. G., & Russell, J. M., III. (2022). Climatology of mesosphere and lower thermosphere residual circulations and mesopause height derived from SABER observations. *Journal of Geophysical Research: Atmospheres*, 127(4), e2021JD035666. <https://doi.org/10.1029/2021JD035666>
- Weimer, D. R. (2005). Improved ionospheric electrodynamic models and application to calculating Joule heating rates. *Journal of Geophysical Research*, 110(A5), A05306. <https://doi.org/10.1029/2004JA010884>
- Yamazaki, Y., Harding, B. J., Qiu, L., Stolle, C., Siddiqui, T. A., Miyoshi, Y., et al. (2023). Monthly climatologies of zonal-mean and tidal winds in the thermosphere as observed by ICON/MIGHTI during April 2020–March 2022. *Earth and Space Science*, 10(6), e2023EA002962. <https://doi.org/10.1029/2023EA002962>
- Yamazaki, Y., & Richmond, A. D. (2013). A theory of ionospheric response to upward-propagating tides: Electrodynamic effects and tidal mixing effects. *Journal of Geophysical Research: Space Physics*, 118(9), 5891–5905. <https://doi.org/10.1002/jgra.50487>
- Yoshikawa, M., & Miyahara, S. (2003). Zonal mean meridional circulation in the low to middle latitude of MLT region: A numerical simulation by a general circulation model. *Advances in Space Research*, 32(5), 709–717. [https://doi.org/10.1016/S0273-1177\(03\)00405-8](https://doi.org/10.1016/S0273-1177(03)00405-8)
- Yue, J., Jian, Y., Wang, W., Meier, R., Burns, A., Qian, L., et al. (2019). Annual and semiannual oscillations of thermospheric composition in TIMED/GUVI limb measurements. *Journal of Geophysical Research: Space Physics*, 124(4), 3067–3082. <https://doi.org/10.1029/2019JA026544>